RSC Advances

PAPER

View Article Online
View Journal | View Issue

Cite this: *RSC Adv.*, 2024, **14**, 10104

Selective electrooxidation of 5-hydroxymethylfurfural at low working potentials promoted by 3D hierarchical $Cu(OH)_2$@Ni_3Co_1-layered double hydroxide architecture with oxygen vacancies†

Qian Wu,[a] Yanqi Xu, *[abc] Cunjun Li,[ab] Wenfeng Zhu,[ab] Hai Wang,[cd] Xinyu Wang,[e] Aimiao Qin,[a] Haiqing Qin[f] and Linjiang Wang *[ab]

Selective electrooxidation of 5-hydroxymethylfurfural (HMF) to 2,5-furandicarboxylic acid (FDCA) is of great significance in the manufacture of fine chemicals, liquid fuels, pharmaceuticals, plastics, *etc.*, but still suffers from the high potential input, resulting in high electricity consumption. Developing active, low-cost and stable electrocatalysts is crucial for this electrochemical reaction at low working potentials. Herein, a three-dimensional (3D) hierarchical $Cu(OH)_2$@Ni_3Co_1-layered double hydroxide architecture with abundant oxygen vacancies (Vo) was synthesized by facile electrodeposition of Ni_3Co_1-LDH nanosheets on copper foam (CF) supported-$Cu(OH)_2$ nanorods (CF/$Cu(OH)_2$@Ni_3Co_1-LDH) for the selective electrooxidation of HMF to FDCA. The 3D hierarchical architecture of the $Cu(OH)_2$ nanorod core loaded with Ni_3Co_1-LDH nanosheet shell facilitates the rapid transfer of charges and exposes more active sites. The synergistic effect of the core–shell nanoarray structure, atomic level dispersion of Ni and Co on LDH laminates, and rich Vo gives 98.12% conversion of HMF, 98.64% yield and 91.71% selectivity for FDCA at a low working potential of 1.0 V *vs.* RHE. In addition, CF/$Cu(OH)_2$@Ni_3Co_1-LDH exhibits superior stability by maintaining 93.26% conversion of HMF, 93.65% yield and 91.57% selectivity of FDCA after eight successive cycles, showing the immense potential of utilizing electrochemical conversion for biomass.

Received 30th January 2024
Accepted 20th March 2024

DOI: 10.1039/d4ra00769g

rsc.li/rsc-advances

Introduction

As a platform molecule from renewable biomass resources, 5-hydroxymethylfurfural (HMF) can be oxidized towards many high value-added fine chemicals, such as 2,5-furandicarboxylic acid (FDCA), 5-hydroxymethyl-2-furancarboxylic acid (HMFCA), 5-formyl-2-furancarboxylic acid (FFCA), *etc.*, which can be considered as one of the promising approaches for reducing the consumption of fossil energy and environmental pollution.[1,2] Electrochemical oxidation of HMF for upgrading of biomass-derived chemicals has attracted widespread interest by virtue of its favourable thermodynamic and kinetic properties, low temperature and atmospheric pressure without the need for oxygen or air.[2–4]

Various nanomaterials have been developed for different electrocatalytic reactions.[5–7] In recent years, Ni- and Co-based catalysts have achieved promising activity, and the Co^{II}/Co^{III} and/or Ni^{II}/Ni^{III} redox species are regarded as the active sites for the direct HMF electrooxidation.[8,9] For example, Ni-based monometallic materials mostly have been studied extensively as HMF oxidation catalysts under the working potentials ≥1.423 V *vs.* RHE.[10–13] Meanwhile, monometallic Co-based catalysts typically were required to deliver an efficient HMF oxidation to FDCA at high potentials ≥1.45 V_{RHE}.[14–17] To date, electrocatalytic transformation of HMF into FDCA has obvious advantages in terms of yield and Faraday efficiency (FE). However, it still requires high potentials input and high

[a]*College of Materials Science and Engineering, Key Laboratory of New Processing Technology for Nonferrous Metal & Materials, Ministry of Education, Guilin University of Technology, Guilin 541004, China. E-mail: xuyanqi@glut.edu.cn; wlinjiang@163.com*

[b]*Collaborative Innovation Center for Exploration of Nonferrous Metal Deposits and Efficient Utilization of Resources, Guilin University of Technology, Guilin 541004, China*

[c]*Guangxi Key Laboratory of Nuclear Physics and Nuclear Technology, Guangxi Normal University, Guilin 541004, China*

[d]*College of Physics and Technology, Guangxi Normal University, Guilin 541004, China*

[e]*School of Materials and Energy, University of Electronic Science and Technology of China, Chengdu 611731, China*

[f]*Guangxi Key Laboratory of Superhard Material, National Engineering Research Center for Special Mineral Material, Guangxi Technology Innovation Center for Special Mineral Material, China Nonferrous Metal (Guilin) Geology and Mining Co., Ltd., Guilin 541004, China*

† Electronic supplementary information (ESI) available. See DOI: https://doi.org/10.1039/d4ra00769g

electricity consumption, which limits its application in industry.[18] The electrooxidation of HMF at low working potentials can reduce side reactions during the electrocatalytic process, improve energy efficiency, and help achieve more sustainable electrocatalytic production.[19]

To boost the electrocatalytic activity, Ni–Co based bimetallic oxides/hydroxides/oxyhydroxides with dual sites form synergism between two metal centers have been constructed, realizing the electrocatalytic oxidation of HMF at low working potentials.[20,21] It has been demonstrated that the synergistic effect of Ni and Co elements in $NiCo_2O_4$ could facilitate HMF electrooxidation, resulting in 90.8% selectivity and 87.5% FE for FDCA, which outperformed its single component of NiO and Co_3O_4 catalysts.[22] β-$Co_xNi_{1-x}(OH)_2$ catalyst fabricated by Co doping on β-$Ni(OH)_2$ manifested an onset potential (1.34 V_{RHE}) for HMF electrooxidation and achieved 96.4% yield for FDCA.[23] NiO–Co_3O_4 nanostructures exhibited HMF oxidation with 98% yield of FDCA at a low onset potential of 1.28 V_{RHE}.[24] Although the working potentials of bimetallic Ni–Co based catalysts catalyzed system are much lower than those of Ni- and Co-based catalysts catalyzed system, it's highly desirable to develop effective catalysts for HMF electrooxidation at more lower working potential (<1.0 V *vs.* RHE). Furthermore, the HMF electrooxidation involved the competitive adsorption of OH^- and HMF on the metal sites, and it has been proved that OH^- could fill into oxygen vacancy (Vo) prior to coupling with HMF through lattice oxygen oxidation process and then accelerate the rate-determining step of the dehydrogenation of HMFCA intermediates to yield FDCA.[25] Thus, Vo-rich electrocatalysts are highly desirable to improve the HMF electrooxidation performance.[26–30]

Contrasted with other oxides/hydroxides/oxyhydroxides, layered double hydroxides (LDHs), with the formula of $[M_{1-x}^{2+}M_x^{3+}(OH)_2]^{x+}(A^{n-})_{x/n}\cdot mH_2O$, where M^{II} and M^{III} represent the divalent and trivalent metal cations (such as Mg^{2+}, Zn^{2+}, Ni^{2+}, Co^{3+}, Fe^{3+}, V^{3+}, Al^{3+}, *etc.*), are a typical two-dimensional (2D) layered structure with the advantages of its multimetallic components and atomic-level dispersion of metallic cations on LDH layers.[31–37] Due to the unique synergistic effect and numerous structural defects (such as Vo, metal vacancies), LDHs have drawn more attention in the sector of small molecules oxidation, such as water, methanol, ethanol, glucose, as well as HMF.[38–42] Practically, the lamellas of LDHs are easy to stack together in the fabrication and electrocatalytic process, which prevents the efficient contact active sites with reactant and thereby limits the electrocatalytic activity. To overcome this issue, plenty of strategies were developed to fabricate LDHs based electrocatalysts with larger surface area and higher exposure of active sites.[43,44] Among these strategies, building LDHs-based hierarchical structures with large surface area, abundant interfaces and fully exposed active sites has been regarded as a promising alternative. In terms of fabricating LDHs-based hierarchical structures, conductive substrates, such as Cu_xS, CuO, $Cu(OH)_2$, *etc.*, usually utilized as cores to grow LDHs shells due to their unique metallic properties. For example, bifunctional Cu_xS@NiCo-LDH core–shell nanoarray electrocatalysts exhibit superior electrocatalytic activity for HMF electrooxidation where a current density of 87 mA cm^{-2} was achieved at 1.30 V *vs.* RHE with FE of nearly 100% for FDCA production, outperforming most of reported Ni/Co-based HMFOR systems.[45] CuO@NiCo-LDH hierarchical structure consisting of NiCo-LDH nanosheets and CuO nanowires was fabricated as electrocatalysts, achieving a high yield (89%) and FE (82%) of FDCA in the HMF electrooxidation due to the numerous active sites and fast electron transport.[46] Therefore, it is highly desirable to develop LDHs-based electrocatalysts with hierarchical structures for selective electrooxidation of HMF at low working potentials, ambient pressure and temperature.

Herein, we designed and successfully fabricated a three-dimensional (3D) hierarchical $Cu(OH)_2$@Ni_3Co_1-LDH architecture on copper foam (CF) (denoted as CF/$Cu(OH)_2$@Ni_3Co_1-LDH) by assembling thin Ni_3Co_1-LDH nanosheets on CF-supported $Cu(OH)_2$ nanorods, which can not only serve as a substrate to provide sufficient conductivity for facilitating carrier transfer but also can serve as a core to provide growth sites for Ni_3Co_1-LDH nanosheets. The as-prepared 3D hierarchical $Cu(OH)_2$@Ni_3Co_1-LDH architecture exhibited excellent electrooxidation of HMF at a low working potential of 1.0 V *vs.* RHE, where a considerable conversion of HMF (98.12%) with high yield (98.64%) and selectivity (91.71%) for FDCA was achieved. Furthermore, $Cu(OH)_2$@Ni_3Co_1-LDH showed superior stability, retaining 93.65% yield and 91.57% selectivity for FDCA after eight successive electrocatalytic cycles. Thus outstanding electrocatalytic performance could be attributed to the excellent electrical conductivity of the $Cu(OH)_2$ nanorods, abundant exposed active sites of the Ni_3Co_1-LDH nanosheets with enriched Vo, and open structure of the hierarchical architecture. This study will provide a promising avenue for utilizing low-cost and active LDHs-based catalysts for the electrochemical synthesis of valuable fine chemicals.

Materials and methods

Materials

Copper foam (CF) was purchased from Kunshan Longsheng Bao Electronic Materials Co., Ltd. 5-Hydroxymethylfurfural (HMF) (95%) was provided by Shanghai Ron Chemical Technology Co., Ltd. HCl (A.R.) and ethanol (A.R.) were obtained from Shantou Xilong Chemical Co., Ltd. NaOH (96%), KOH (85%), $(NH_4)_2S_2O_8$ (98.5%), and $Ni(NO_3)_2\cdot 6H_2O$ (98%) were bought from Xilong Chemical Reagent Co., Ltd. $Co(NO_3)_2\cdot 6H_2O$ (99%) was offered in Rhawn Chemical Reagent Co., Ltd.

Preparation of CF/$Cu(OH)_2$@NiCo-LDH architectures

Firstly, CF with 1 × 2 cm^2 was sonicated sequentially with ethanol, 3.0 M HCl, and deionized water for 5 min and dried at 60 °C. Then, 0.2 mol NaOH and 0.01 mol $(NH_4)_2S_2O_8$ were dissolved in 100 mL deionized water to form a homogeneous solution. The pre-treated CF was then put into the above solution for 15 minutes and allowed to generate $Cu(OH)_2$ nanorods on the CF surface. The obtained sample (denoted as CF/$Cu(OH)_2$) was washed repeatedly with ethanol and deionized water, and then dried at 70 °C.

The NiCo layered double hydroxide (NiCo-LDH) nanosheets were deposited on CF/$Cu(OH)_2$ by electrodeposition method.[47] In the typical process, the CF/$Cu(OH)_2$ was used as the working electrode, the saturated calomel electrode (SCE) and the Pt sheet were used as the reference electrode and the counter electrode to form a three-electrode system. The electrodeposition process was carried out at −1.0 V for 600 s in an electrolyte system containing $Ni(NO_3)_2 \cdot 6H_2O$ (0.0375 M) and $Co(NO_3)_2 \cdot 6H_2O$ (0.0125 M). The obtained electrode material (denoted as CF/$Cu(OH)_2$@Ni_3Co_1-LDH) was rinsed with deionized water and dried at 60 °C under vacuum. The synthesis of the CF/$Cu(OH)_2$@NiCo-LDH with different Ni/Co molar ratios (Ni/Co = 2 and 4) were performed through the same method by changing the amount of $Ni(NO_3)_2 \cdot 6H_2O$ and $Co(NO_3)_2 \cdot 6H_2O$ raw materials. In addition, the synthesis of CF/Ni_3Co_1-LDH, CF/$Cu(OH)_2$@$Ni(OH)_2$ and CF/$Cu(OH)_2$@$Co(OH)_2$ were following as the process of deposition NiCo-LDH on CF/$Cu(OH)_2$.

Characterization

The crystal structure of the samples was characterized by X-ray diffraction (XRD), the morphologies of the materials were observed by field emission scanning electron microscopy (SEM, Hitachi S4800), and the lattice fringes of the materials were measured by high-resolution transmission electron microscopy (HRTEM, 200 kV). X-ray photoelectron spectroscopy (XPS) analysis of surface electronic states was using the Thermo Scientific K-Alpha X-ray photoelectron spectrometer. Using a Thermo Nicolet NEXUS 670, Fourier transform infrared spectroscopy (FT-IR) spectra were captured in the 400–4000 cm^{-1} range.

Electrochemical measurements

A three-electrode electrochemical workstation (Shanghai Chenhua CHI660E) was used for electrochemical measurement with Pt mesh as the counter electrode, CF/$Cu(OH)_2$@NiCo-LDH as the working electrode, and the SCE electrode as the reference electrode. In 1.0 M KOH and 1.0 M KOH + 10 mM HMF solutions, cyclic voltammetry (CV) and linear scanning voltammetry (LSV) measurements were performed with a scanning rate of 50 mV s^{-1} and a potential range of −0.6 to 1.3 V. The electrochemical impedance spectroscopy (EIS) was measured in range of 100 kHz to 0.01 Hz under open circuit potential, and the electrochemical active surface area (ECSA) was measured in 1.0 M KOH + 10 mM HMF electrolyte by the CV at the potential window of 0.15–0.25 V with the scan rates of 2 to 10 mV s^{-1}, and the calculation equation can be described as ECSA = C_{dl}/C_s (where C_s is the specific capacitance of the sample). The potential value obtained from the SCE electrode was converted to the reversible hydrogen electrode (RHE) scale using the formula of E (*vs.* RHE) = E (*vs.* SCE) + 0.24 + 0.059 pH.

Electrochemical oxidation of 5-hydroxymethylfurfural

Electrochemical oxidation of HMF was carried out in an H-type cell separated by N117 proton exchange membrane (Sigma-Aldrich) at room temperature. In the typical three-electrode system, CF/$Cu(OH)_2$@Ni_3Co_1-LDH was used as the working electrode (anode), Pt mesh was applied as the counter electrode (cathode), and the SCE electrode was used as the reference electrode. The reaction was conducted in 35.0 mL of 1.0 M KOH electrolyte with 10 mM HMF at a series of onset potentials (0.2–1.51 V *vs.* RHE) and room temperature for 3 h. High performance liquid chromatography (HPLC, Thermo Scientific U 3000) with a C18 (2) column and an ultraviolet-visible detector set at 278 nm was used to detect the concentration change of HMF and its oxidative products during the electrochemical reaction. Acetonitrile and the aqueous acetic acid solution with a mass fraction of 0.1% (5 : 95) was used as the mobile phase with a flow rate of 1.0 mL min^{-1}. The conversion rate of HMF, the yield, selectivity, and Faraday Efficiency (FE) of FDCA were calculated as follows:

$$\text{HMF conversion rate} = \frac{\text{consumed mol of HMF}}{\text{initial mol of HMF}} \times 100\%$$

$$\text{FDCA yield} = \frac{\text{formed mol of FDCA}}{\text{initial mol of HMF}} \times 100\%$$

$$\text{FDCA selectivity} = \frac{\text{formed mol of FDCA}}{\text{consumed mol of HMF}} \times 100\%$$

$$\text{FDCA FE} = \frac{F \times n \times \text{formed mol of FDCA}}{\text{initial mol of HMF}} \times 100\%$$

where F = 96 485 C mol^{-1} and n = 6.

Results and discussion

The synthetic route of 3D hierarchical CF/$Cu(OH)_2$@Ni_3Co_1-LDH architecture is shown in Scheme 1. Firstly, $Cu(OH)_2$ nanorods were grown on conductive CF substrate by wet oxidation according to the chemical reaction equation: $Cu + 4NaOH + (NH_4)_2S_2O_8 \rightarrow Cu(OH)_2 + 2Na_2SO_4 + 2NH_3 + 2H_2O$.[48] Then, the Ni_3Co_1-LDH nanosheets were generated on $Cu(OH)_2$ nanorods by electrodeposition to form the target architecture (*e.g.* CF/$Cu(OH)_2$@Ni_3Co_1-LDH). The characterizations, including XRD, SEM, TEM, XPS, *etc.*, were utilized to depict the structural features of the as-synthesized materials. As shown in Fig. 1a, there are two characteristic diffractions at 43.3° and 50.43°, 74.1° in the XRD patterns of all samples, which can correspond to the (111), (200), (220) crystal planes of CF (JCPDS

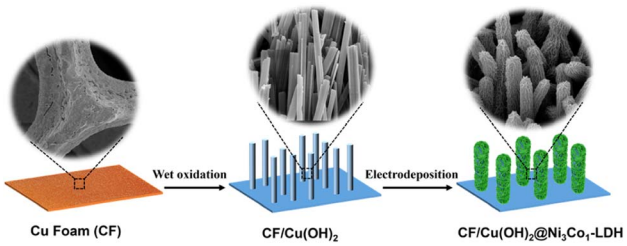

Scheme 1 Schematic synthetic route of 3D hierarchical CF/$Cu(OH)_2$@Ni_3Co_1-LDH architectures.

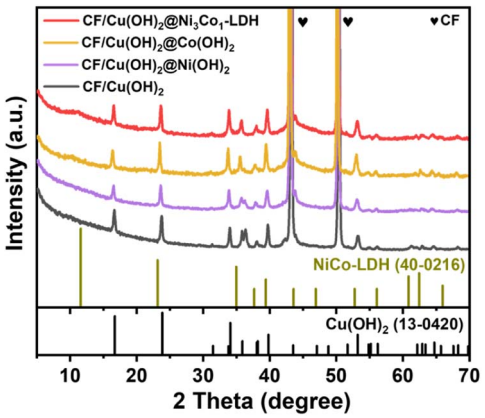

Fig. 1 XRD patterns of CF/$Cu(OH)_2$, CF/$Cu(OH)_2$@$Ni(OH)_2$, CF/$Cu(OH)_2$@$Co(OH)_2$, and CF/$Cu(OH)_2$@Ni_3Co_1-LDH, respectively.

04-0836). For CF/$Cu(OH)_2$, the reflections at 16.7°, 23.8°, 34.1°, 35.9°, 39.8°, 48.7°, and 53.4° can be assigned to (020), (021), (002), (111), (130), (042), and (132) crystal planes, indicating that $Cu(OH)_2$ nanorods have been successfully synthesized on the CF substrate.[49] Due to the growth orientation, low crystallinity and/or less content, only one weak diffraction peak at 11.3° corresponding to the (003) crystal plane of typical LDHs can be detected in the XRD pattern of CF/$Cu(OH)_2$@Ni_3Co_1-LDH.[50,51] Similarly, barely detectable reflections for $Ni(OH)_2$, $Co(OH)_2$, and Ni_3Co_1-LDH can be observed in the XRD patterns of the control samples (*e.g.* CF/$Cu(OH)_2$@$Ni(OH)_2$, CF/$Cu(OH)_2$@$Co(OH)_2$, and CF/Ni_3Co_1-LDH (Fig. S1†).

The morphologies and microstructures of the materials were characterized by SEM and HRTEM images. It can be seen from the SEM image of CF/$Cu(OH)_2$ that rod-like $Cu(OH)_2$ nanorods with an average diameter of about 200 nm were grown on the surface of CF (Fig. S1a†). For CF/$Cu(OH)_2$@Ni_3Co_1-LDH, the $Cu(OH)_2$ nanorods are tightly wrapped by uniformly growing Ni_3Co_1-LDH nanosheets, which are thin and dense in size to form a uniform hierarchical structure (Fig. 2a and c). In this hierarchical structure, $Cu(OH)_2$ nanorods as core can improve the conductivity, while the Ni_3Co_1-LDH nanosheets with large surface area and high porosity can provide numerous active sites to facilitate electron transport for subsequent electrocatalytic reactions. Furthermore, element mapping diagram (EDS) shows that Cu, Ni, Co, and O are evenly distributed in CF/$Cu(OH)_2$@Ni_3Co_1-LDH (Fig. 2b), suggesting that Ni_3Co_1-LDH nanosheets are uniformly distributed on the $Cu(OH)_2$ nanorods. Moreover, HRTEM images were utilized to reveal the microstructure of CF/$Cu(OH)_2$@Ni_3Co_1-LDH. As shown in Fig. 2d, the lattice fringes with *d*-spacings of 0.232 nm and 0.251 nm could be assigned to the (015) crystal plane of NiCo-LDH (JCPDS 40-0216) and the (111) crystal plane of $Cu(OH)_2$ (JCPDS 13-0420), respectively. Interestingly, without $Cu(OH)_2$ nanorods as supporting core, Ni_3Co_1-LDH nanosheets can't be grown directly on the CF surface (Fig. S2b†). For the control materials (*e.g.* CF/$Cu(OH)_2$@$Ni(OH)_2$ and CF/$Cu(OH)_2$@$Co(OH)_2$), the generated $Ni(OH)_2$ showed unevenly agglomerated nanorods, while $Co(OH)_2$ showed thin flakes without rod-like structures (Fig. S2c and d†), suggesting that synergistic effect between binary or multi-component significantly affect the morphology. In order to explore the impact of the Ni/Co molar ratio on the structure and morphologies of CF/$Cu(OH)_2$@NiCo-LDH, CF/$Cu(OH)_2$@Ni_xCo_y-LDH (x/y = 2/1, 3/1, 4/1) were synthesized. According to the SEM images (Fig. S3†) and electrochemical measurements (Fig. S4†), CF/$Cu(OH)_2$@Ni_3Co_1-LDH shows more uniform morphology and better electrochemical activity of HMF electrooxidation. Moreover, to explore the effect of electrodeposition time on the dispersion and surface structure of Ni_3Co_1-LDH nanosheets on CF/$Cu(OH)_2$ nanoarrays, the electrodeposition time was adjusting to be 450 s, 600 s, and 750 s. As shown in Fig. S5,† uniform dispersion of Ni_3Co_1-LDH nanosheets on $Cu(OH)_2$ nanorods could be achieved when deposition time was 600 s. The electrochemical measurements indicated that CF/$Cu(OH)_2$@Ni_3Co_1-LDH prepared at 600 s showed the best activity of HMF electrooxidation (Fig. S6†). Based on the above, the Ni/Co molar ratio and the electrodeposition time for synthesizing CF/$Cu(OH)_2$@NiCo-LDH architecture were determined to be 3/1 and 600 s.

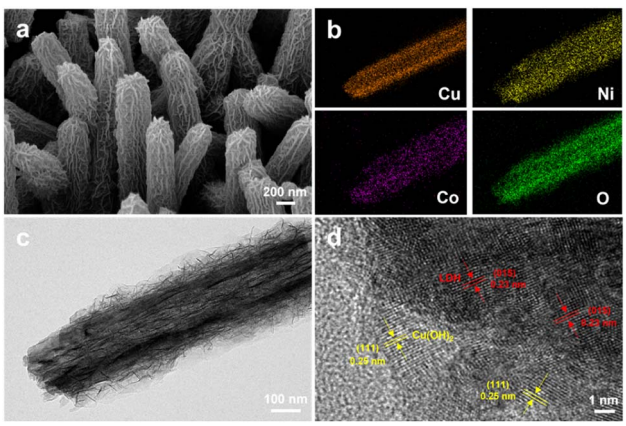

Fig. 2 (a) SEM image, (b) elemental mappings, (c) TEM image and (d) HRTEM image of CF/$Cu(OH)_2$@Ni_3Co_1-LDH.

To clarify the interaction between the Ni_3Co_1-LDH nanosheets and $Cu(OH)_2$ nanorods, X-ray photoelectron spectroscopy (XPS) measurements were carried out to analyze the materials' chemical makeup and surface electronic state (Fig. 3). The full survey spectrum of the synthesized CF/$Cu(OH)_2$@Ni_3Co_1-LDH confirms the coexistence of Cu, O, Ni and Co elements (Fig. 3a). As depicted in Fig. 3b, high-resolution Ni 2p spectra of CF/$Cu(OH)_2$@Ni_3Co_1-LDH exhibit two peaks of Ni $2p_{3/2}$ and Ni $2p_{1/2}$ combined with satellites at 861.7 and 880.2 eV. Two fitting peaks at 856.1 and 873.4 eV can be classified as Ni^{2+} and two fitting peaks at 858.0 and 875.2 eV can be classified as Ni^{3+}, suggesting the coexistence of Ni^{2+} and Ni^{3+}. It is worth noting that the binding energy of Ni in CF/$Cu(OH)_2$@Ni_3Co_1-LDH is shifted by 0.20 eV in the negative direction compared with CF/$Cu(OH)_2$@$Ni(OH)_2$, indicating that incorporating Co element results in the reduction of valence state of Ni. As shown in high-resolution Co 2p spectra of CF/$Cu(OH)_2$@Ni_3Co_1-LDH (Fig. 3c), two peaks classified as Co^{3+} are fitted at 780.8 and 796.5 eV, and two peaks classified as Co^{2+} are

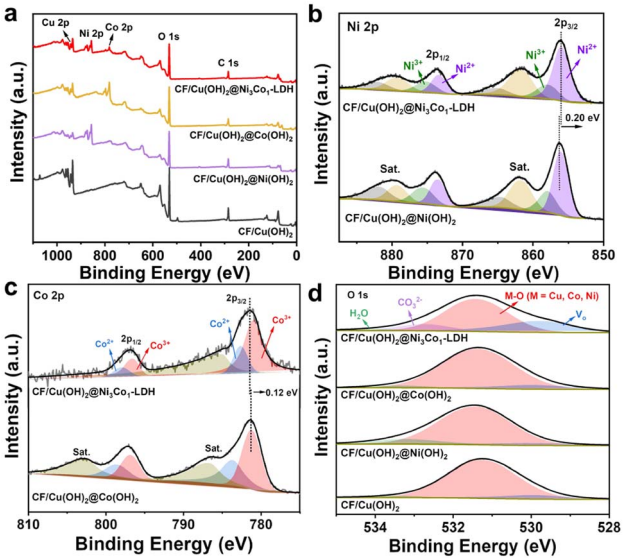

Fig. 3 (a) Survey spectra and (d) O 1s spectra of CF/$Cu(OH)_2$, CF/$Cu(OH)_2$@$Ni(OH)_2$, CF/$Cu(OH)_2$@$Co(OH)_2$, and CF/$Cu(OH)_2$@Ni_3Co_1-LDH, respectively; (b) Ni 2p spectra of CF/$Cu(OH)_2$@Ni_3Co_1-LDH and CF/$Cu(OH)_2$@$Ni(OH)_2$; (c) Co 2p spectra of CF/$Cu(OH)_2$@Ni_3Co_1-LDH and CF/$Cu(OH)_2$@$Co(OH)_2$.

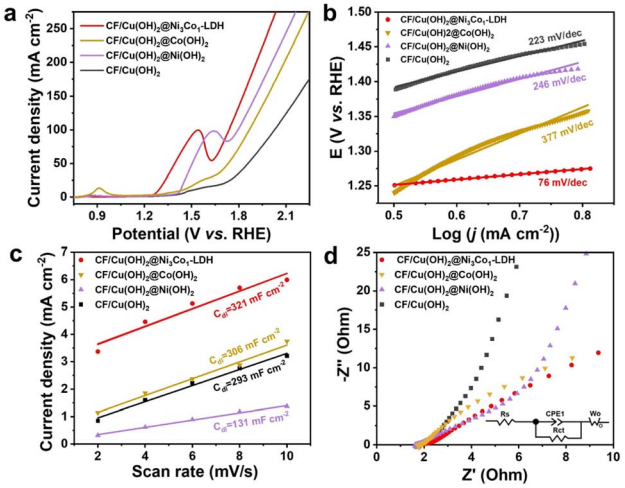

Fig. 4 (a) LSV curves at a scan rate of 50 mV s^{-1}, (b) Tafel, (c) C_{dl} and (d) EIS spectra of CF/$Cu(OH)_2$, CF/$Cu(OH)_2$@$Ni(OH)_2$, CF/$Cu(OH)_2$@$Co(OH)_2$ and CF/$Cu(OH)_2$@Ni_3Co_1-LDH in 1.0 M KOH with 10 mM HMF.

fitted at 782.7 and 797.3 eV, demonstrating the coexistence of Co^{2+} and Co^{3+}. Compared to the Co 2p spectra of CF/$Cu(OH)_2$@$Co(OH)_2$, the binding energy of Co in CF/$Cu(OH)_2$@Ni_3Co_1-LDH is shifted by 0.12 eV in the negative direction, indicating that the valence state of Co element increases due to the introduction of Ni element. Besides, the peak at 532.9 eV in the O 1s spectra of CF/$Cu(OH)_2$@Ni_3Co_1-LDH can be corresponding to CO_3^{2-}, which matches those reported LDHs materials containing interlaminar carbonate anions. Three distinct components assigned to oxygen vacancy (Vo), M–O (M = Cu, Co, Ni), and absorbed H_2O could be seen in the O 1s spectra for CF/$Cu(OH)_2$, CF/$Cu(OH)_2$@$Ni(OH)_2$, CF/$Cu(OH)_2$@$Co(OH)_2$, and CF/$Cu(OH)_2$@Ni_3Co_1-LDH (Fig. 3d). Furthermore, the fitting area of Vo in CF/$Cu(OH)_2$@Ni_3Co_1-LDH is larger than those in the regarded as active sites. Based on the provided experimental evidence and discussion, the 3D hierarchical CF/$Cu(OH)_2$@Ni_3Co_1-LDH architecture with abundant interface and Vo not only promoting the generation and exposure of active sites but also providing interfacial structure between $Cu(OH)_2$ and Ni_3Co_1-LDH to facilitate the electron transport during the electrocatalytic reaction, which will have an impact on improving the selectively electrochemical oxidation of HMF.

Inspired by the expected 3D hierarchical structure of CF/$Cu(OH)_2$@Ni_3Co_1-LDH, a series experiments of electrooxidation of HMF were measured in an alkaline environment. The linear sweep voltammetry (LSV) curves of CF/$Cu(OH)_2$, CF/$Cu(OH)_2$@$Ni(OH)_2$, CF/$Cu(OH)_2$@$Co(OH)_2$ and CF/$Cu(OH)_2$@Ni_3Co_1-LDH obtained in 1.0 M KOH with 10 mM HMF were shown in Fig. 4a, and it's evident that CF/$Cu(OH)_2$@Ni_3Co_1-LDH exhibited superiors electrocatalytic activity than other samples. The electrochemical performance of CF/$Cu(OH)_2$@Ni_3Co_1-LDH in 1 M KOH with and without HMF was evaluated. Fig. S7† showed that CF/$Cu(OH)_2$@Ni_3Co_1-LDH exhibited much higher activity in 1.0 M KOH with HMF than in pure 1.0 M KOH electrolytes, demonstrating that the oxidation of HMF occurred at a lower potential in comparison with that for water oxidation. It's worth noting that the LSV and CV curves obtained in the presence of HMF showed a little broader than those curves obtained in the absence of HMF, due to the direct HMF oxidation on the catalysts surface at potentials between the Co/Ni redox peak and the onset of water oxidation. This result implies that the CF/$Cu(OH)_2$@Ni_3Co_1-LDH electrode exhibits a greater preference for HMF oxidation over water oxidation.[17,52–54] To explore the superior HMF oxidation, Tafel plots were applied to study the reaction kinetics (Fig. 4b). The CF/$Cu(OH)_2$@Ni_3Co_1-LDH exhibited much lower Tafel slope (76 mA dec^{-1}) than those of CF/$Cu(OH)_2$ (223 mA dec^{-1}), CF/$Cu(OH)_2$@$Ni(OH)_2$ (246 mA dec^{-1}), and CF/$Cu(OH)_2$@$Co(OH)_2$ (377 mA dec^{-1}), suggesting the lowest reaction barrier and faster electrocatalytic kinetics, which could be ascribed to the synergistic effect of Ni and Co sites and electronic interaction between Ni and Co species played a significant role in increasing intrinsic activity and boosting the HMF oxidation kinetics. The electrochemical double layer capacitance (C_{dl}) was used to measure the electrochemical surface area (ECSA), where C_{dl} was obtained by CV ranging from 1.22 to 1.32 V at different scan rates (2, 4, 6, 8, and 10 mV s^{-1}) (Fig. S8†). As shown in Fig. 4c, CF/$Cu(OH)_2$@Ni_3Co_1-LDH possessed the largest C_{dl} of 321 mF cm^{-2}, which was higher than those of CF/$Cu(OH)_2$ (293 mF cm^{-2}), CF/$Cu(OH)_2$@$Ni(OH)_2$ (131 mF cm^{-2}), and CF/$Cu(OH)_2$@$Co(OH)_2$ (306 mF cm^{-2}). The higher ECSA leads to the decline of working potential and the enhancement of HMF oxidation performance. Moreover, electrochemical impedance spectroscopy (EIS) measurements were used to elucidate charge transfer of the catalysts. As shown in Fig. 4d of the electrochemical impedance spectra (EIS), the semicircle of CF/$Cu(OH)_2$@Ni_3Co_1-LDH is the smallest than that of other

catalysts, suggesting that the electron transfer rate was faster and significantly improved the activity of HMFOR. To further dissect the EIS data it has been fitted and the fitted results (Table S1†) illustrated that the charge transfer resistance (R_{ct}) of CF/Cu(OH)$_2$@Ni$_3$Co$_1$-LDH (0.34 Ω cm^2) was lower than those of CF/Cu(OH)$_2$ (0.51 Ω cm^2), CF/Cu(OH)$_2$@Ni(OH)$_2$ (0.48 Ω cm^2) and CF/Cu(OH)$_2$@Co(OH)$_2$ (0.49 Ω cm^2), proven faster electron transportation on the CF/Cu(OH)$_2$@Ni$_3$Co$_1$-LDH with excellent electrochemical performance.[55–57] Such an improved electrochemical performance of CF/Cu(OH)$_2$@Ni$_3$Co$_1$-LDH in comparison to other samples was derived from 3D hierarchical architecture, oxygen vacancies (Vo), as well as synergistic effect between Co species and Ni species.[45]

To explore the conversion of HMF and the yield and selectivity of FDCA over CF/Cu(OH)$_2$@Ni$_3$Co$_1$-LDH, the electrooxidation of HMF were performed in an H-type electrolyzer, where the anodic cell containing 1.0 M KOH with 10 mM HMF. During the electrocatalytic process, the concentrations of HMF and its oxidative products were monitored by high performance liquid chromatography (HPLC) (Fig. S9†), and the conversion of HMF and the yield and selectivity of its oxidative products were evaluated by an external standard method (Fig. S10†). As shown in Fig. 5a, the HMF conversion, as well as yield and selectivity of FDCA, over different catalysts at an applied potential of 1.0 V *vs.* RHE in 1.0 M KOH containing 10 mM HMF under room temperature were investigated. It can be seen that the HMF conversion, yield and selectivity of FDCA were detected to be 98.12%, 98.64%, and 91.71% for CF/Cu(OH)$_2$@Ni$_3$Co$_1$-LDH, which shows higher activity for HMF electrooxidation than those of CF/Cu(OH)$_2$, CF/Cu(OH)$_2$@Ni(OH)$_2$, and CF/Cu(OH)$_2$@Co(OH)$_2$, respectively, and the fast electron transfer contributed to the favourable electrocatalytic performance of CF/Cu(OH)$_2$@Ni$_3$Co$_1$-LDH for HMFOR. Similarly, CF/Cu(OH)$_2$@Ni$_3$Co$_1$-LDH catalyzed system was more effective than CF and CF/@Ni$_3$Co$_1$-LDH (Fig. S11†). As depicted in Fig. 5b, the concentration of HMF decreased and the level of FDCA increased with the increasing time, proving that HMF was successfully converted to FDCA. Observe that whilst concentration fluctuations of HMFCA and FFCA were noticeable, 2,5-diformylfuran (DFF) is hardly present. This indicates that FDCA is most likely produced by following the path of HMFCA intermediate (Fig. S12†).[11,12,58,59] In addition, the as-prepared CF/Cu(OH)$_2$@Ni$_3$Co$_1$-LDH is comparable to the previously reported HMF oxidation electrodes (Table S2†). The superior electrochemical activity of CF/Cu(OH)$_2$@Ni$_3$Co$_1$-LDH could be attributed to good conductivity, 3D hierarchical architecture, and abundant Vo. Hence, the CF/Cu(OH)$_2$@Ni$_3$Co$_1$-LDH was selected to investigate the electrochemical performance of HMF oxidation.

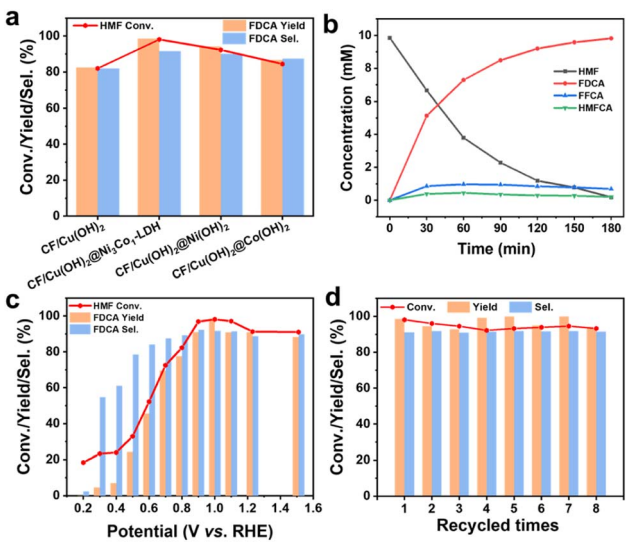

Fig. 5 (a) The HMF conversion, yield and selectivity of FDCA obtained over CF/Cu(OH)$_2$, CF/Cu(OH)$_2$@Ni$_3$Co$_1$-LDH, CF/Cu(OH)$_2$@Ni(OH)$_2$, and CF/Cu(OH)$_2$@Co(OH)$_2$, respectively. (b) Concentration HMF and its oxidative products *versus* reaction time, and (c) the HMF conversion, yield and selectivity of FDCA obtained at different working potentials over CF/Cu(OH)$_2$@Ni$_3$Co$_1$-LDH. (d) The HMF conversion, FDCA yield and selectivity over CF/Cu(OH)$_2$@Ni$_3$Co$_1$-LDH under eight successive cycles. Reaction conditions: 35 mL of 10 mM HMF, 25 °C, onset potential 1.0 V *vs.* RHE, and reaction time 3 h.

The low-potential aldehyde oxidation reaction is key to the electrocatalytic system. As such, the electrooxidation of HMF at various working potentials were conducted in this study (Fig. 5c). Increasing the working potential from 0.2 to 1.51 V *vs.* RHE leads to increase of HMF conversion, as well as yield and selectivity of FDCA, that reaches a maximum at 1.0 V *vs.* RHE. It's worth noting that the products of HMF oxidation at low potential (0.2 V *vs.* RHE) differ from those at higher potentials where HMFCA with a selectivity of 93.89% is the dominating product due to the HMFCA may be directly generated from a non-faradaic process (Fig. S13†).[60] On applying working potentials of 0.3–1.51 V *vs.* RHE, FDCA is the main product, with small amounts of HMFCA and FFCA as oxidative intermediates, due to the hydroxymethyl and aldehyde groups of HMF are oxidized into carboxylic groups.[58] The HMF conversion, yield and selectivity of FDCA in the optimum potential (1.0 V *vs.* RHE) are calculated to be 98.12%, 98.64%, and 91.71%, respectively. In addition, the calculated FE towards FDCA is 86.5%. These results demonstrate that the aldehyde group of HMF can be selectively oxidized to a carboxylic group over the CF/Cu(OH)$_2$@Ni$_3$Co$_1$-LDH electrocatalyst at low working potentials. The stability of the catalyst is of great significance for its practical applications. As such, the CF/Cu(OH)$_2$@Ni$_3$Co$_1$-LDH was used as electrode to study the durability. As shown in Fig. 5d, 93.26% conversion of HMF, 93.65% yield and 91.57% selectivity of FDCA remained in the eighth cycle, indicating that CF/Cu(OH)$_2$@Ni$_3$Co$_1$-LDH shows excellent stability for electrooxidation of HMF. From the XRD patterns (Fig. 6a), CF/Cu(OH)$_2$@Ni$_3$Co$_1$-LDH after recycled measurements (denoted as Re-CF/Cu(OH)$_2$@Ni$_3$Co$_1$-LDH) displays the characteristic peaks as with the fresh one, confirming that the electrocatalyst remained structural stable. Meanwhile, there were no new organic or inorganic functional groups generated after the electrooxidation from FT-IR spectra (Fig. 6b). SEM images demonstrate that the morphology of the catalysts is consistent before and after the electrooxidation (Fig. 6c and d). Considering that the oxidation process of HMF mainly occurs on the surface of the electrocatalyst, the surface properties of Re-CF/

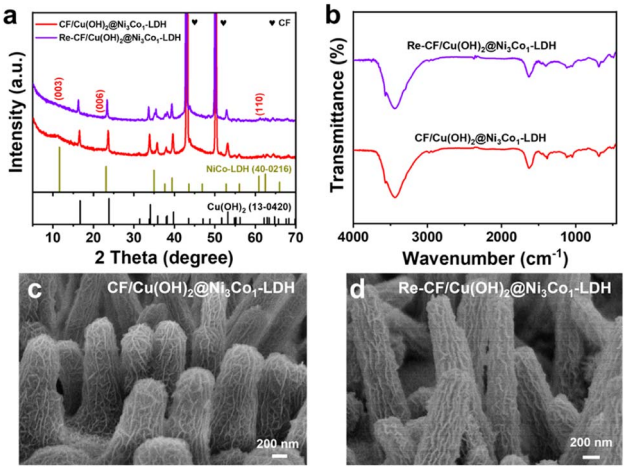

Fig. 6 (a) XRD patterns and (b) FT-IR spectra of CF/$Cu(OH)_2$@Ni_3Co_1-LDH and Re-CF/$Cu(OH)_2$@Ni_3Co_1-LDH. SEM images of (c) CF/$Cu(OH)_2$@Ni_3Co_1-LDH and (d) Re-CF/$Cu(OH)_2$@Ni_3Co_1-LDH.

$Cu(OH)_2$@Ni_3Co_1-LDH were further characterized using XPS (Fig. S14†). Similar peaks to those seen for the fresh electrode were visible in the XPS complete spectra (Fig. S14a†). In the Ni 2p region (Fig. S14b†), the binding energies of Ni in Re-CF/$Cu(OH)_2$@Ni_3Co_1-LDH shows a clearly negative shift of 0.4 eV compared with that of CF/$Cu(OH)_2$@Ni_3Co_1-LDH, which can be credited to the Ni^{3+}/Ni^{2+} redox during the electrocatalytic process. In the Co 2p region (Fig. S14c†), the binding energy of Co in Re-CF/$Cu(OH)_2$@Ni_3Co_1-LDH significantly shifts to lower binding energy compared with that of CF/$Cu(OH)_2$@Ni_3Co_1-LDH, which can be assigned to the formation of CoOOH that has been reported to be the direct active mediator in the oxidation reaction.[61] In the O 1s region (Fig. S14d†), the concentration of Vo decreased after the electrooxidation, suggesting that Vo as an important role were involved in the electrooxidation of HMF.[25–28,38] These results elucidate that the impetus of redox cycle of Ni^{3+}/Ni^{2+} and Co^{3+}/Co^{2+}, as well as Vo, facilitates the HMF oxidation and achieves high durability.

Based on the above experimental results, a schematic diagram of the electrooxidation process of HMF on CF/$Cu(OH)_2$@Ni_3Co_1-LDH is proposed (Fig. S15†). Due to the synergistic interaction of Ni, Co, and Vo, the electrooxidation of HMF towards FDCA is most likely going to follow the path of HMFCA intermediate: the aldehyde group of HMF is preferentially adsorbed on the catalyst surface in the strong alkaline electrolyte (1 M KOH), and an addition reaction occurs under the action of OH^- and water to form intermediate specie; subsequently, the above intermediate specie was dehydrogenated to form the intermediate HMFCA; then the hydroxymethyl group of HMFCA was dehydrogenated to form FFCA; the nucleophilic addition and dehydrogenation of FFCA occurred to proceed to the target product of FDCA.

Conclusions

In summary, we successfully synthesized CF/$Cu(OH)_2$@Ni_3Co_1-LDH with core–shell hierarchical structure by wet oxidation combined with electrodeposition. Benefitting from good electrical conductivity, bimetallic synergistic actions of Ni and Co, abundant Vo, and 3D hierarchical structures, CF/$Cu(OH)_2$@Ni_3Co_1-LDH architecture exhibits excellent electrochemical performance for HMF oxidation. Especially, 98.12% conversion of HMF, 98.64% yield and 91.71% selectivity for FDCA over CF/$Cu(OH)_2$@Ni_3Co_1-LDH was performed at the onset potential of 1.0 V *vs.* RHE. Moreover, CF/$Cu(OH)_2$@Ni_3Co_1-LDH show excellent electrochemical stability, where the yield and selectivity of FDCA remained at 93.7% and 91.6% in the eight electrocatalytic cycle. This Vo -rich architecture catalysts present a novel and energy-efficient solution to obtain upgraded biochemicals.

Author contributions

Conceptualization, Q. W.; methodology, Q. W.; software, Q. W. and Y. X.; validation, C. L., W. Z., H. W., and X. W.; formal analysis, Q. W.; investigation, Q. W., Y. X., C. L., W. Z., H. W., X. W., A. Q., and H. Q.; resources, Y. X. and L. W.; data curation, Q. W.; writing—original draft preparation, Q. W.; writing—review & editing, Y. X.; visualization, X. W.; supervision, Y. X.; project administration, L. W.; funding acquisition, Y. X. and L. W. All authors have read and agreed to the published version of the manuscript.

Conflicts of interest

The authors declare no conflict of interest.

Acknowledgements

This research was supported by the National Natural Science Foundation of China (No. 42062003), the Guangxi Natural Science Foundation (No. 2023GXNSFBA026183), the Research Foundation of State Key Laboratory of Chemical Resource Engineering (No. CRE-2022-01-01), the Research Foundation of Key Laboratory of New Processing Technology for Nonferrous Metal & Materials, Ministry of Education/Guangxi Key Laboratory of Optical and Electronic Materials and Devices (No. 22KF-23, No. 22AA-6, No. 23AA-6), the Open Project of Guangxi Key Laboratory of Nuclear Physics and Nuclear Technology (No. NLK2022-08), the Research Foundation of Guangxi Key Laboratory of Superhard Material, National Engineering Research Center for Special Mineral Material, Guangxi Technology Innovation Center for Special Mineral Material (No. 2023-K-01).

References

1 O. Simoska, Z. Rhodes, S. Weliwatte, J. R. Cabrera-Pardo, E. M. Gaffney, K. Lim and S. D. Minteer, *ChemSusChem*, 2021, **14**, 1674–1686.
2 H. Zhou, Y. Ren, B. Yao, Z. Li, M. Xu, L. Ma, X. Kong, L. Zheng, M. Shao and H. Duan, *Nat. Commun.*, 2023, **14**, 5621.
3 H. Zhou, Z. Li, L. Ma and H. Duan, *Chem. Commun.*, 2022, **58**, 897–907.

4 S. R. Kubota and K.-S. Choi, *ChemSusChem*, 2018, **11**, 2138–2145.
5 Z. Liu, D. Sun, C. Wang, B. You, B. Li, J. Han, S. Jiang, C. Zhang and S. He, *Coord. Chem. Rev.*, 2024, **502**, 215612.
6 D. Qu, S. He, L. Chen, Y. Ye, Q. Ge, H. Cong, N. Jiang and Y. Ha, *Front. Chem.*, 2022, **10**, 1055865.
7 C. Du, P. Li, Z. Zhuang, Z. Fang, S. He, L. Feng and W. Chen, *Coord. Chem. Rev.*, 2022, **466**, 214604.
8 B. Zhang, Z. Li, Y. Zhou, Z. Yang, Z. Xue and T. Mu, *Small*, 2023, 2306663.
9 Y. Lu, C.-L. Dong, Y.-C. Huang, Y. Zou, Z. Liu, Y. Liu, Y. Li, N. He, J. Shi and S. Wang, *Angew. Chem., Int. Ed.*, 2020, **59**, 19215–19221.
10 G. Grabowski, J. Lewkowski and R. Skowroński, *Electrochim. Acta*, 1991, **36**, 1995.
11 B. You, N. Jiang, X. Liu and Y. Sun, *Angew. Chem., Int. Ed.*, 2016, **55**, 9913–9917.
12 S. Barwe, J. Weidner, S. Cychy, D. M. Morales, S. Dieckhöfer, D. Hiltrop, J. Masa, M. Muhler and W. Schuhmann, *Angew. Chem., Int. Ed.*, 2018, **57**, 11460–11464.
13 Y. Meng, S. Yang and H. Li, *ChemSusChem*, 2022, **15**, e202102581.
14 N. Jiang, B. You, R. Boonstra, I. M. Terrero Rodriguez and Y. Sun, *ACS Energy Lett.*, 2016, **1**, 386–390.
15 Z. Zhou, C. Chen, M. Gao, B. Xia and J. Zhang, *Green Chem.*, 2019, **21**, 6699–6706.
16 P. Zhang, X. Sheng, X. Chen, Z. Fang, J. Jiang, M. Wang, F. Li, L. Fan, Y. Ren, B. Zhang, B. J. J. Timmer, M. S. G. Ahlquist and L. Sun, *Angew. Chem., Int. Ed.*, 2019, **58**, 9155–9159.
17 B. Zhu, C. Chen, L. Huai, Z. Zhou, L. Wang and J. Zhang, *Appl. Catal., B*, 2021, **297**, 120396.
18 J. Cai, K. Li and S. Wu, *Biomass Bioenergy*, 2022, **158**, 106358.
19 L. Gao, X. Wen, S. Liu, D. Qu, Y. Ma, J. Feng, Z. Zhong, H. Guan and L. Niu, *J. Mater. Chem. A*, 2022, **10**, 21135–21141.
20 X. Deng, M. Li, Y. Fan, L. Wang, X.-Z. Fu and J.-L. Luo, *Appl. Catal., B*, 2020, **278**, 119339.
21 Z. Zhao, T. Guo, X. Luo, X. Qin, L. Zheng, L. Yu, Z. Lv, D. Ma and H. Zheng, *Catal. Sci. Technol.*, 2022, **12**, 3817–3825.
22 Y. Yang, W. H. Lie, R. R. Unocic, J. A. Yuwono, M. Klingenhof, T. Merzdorf, P. W. Buchheister, M. Kroschel, A. Walker, L. C. Gallington, L. Thomsen, P. V. Kumar, P. Strasser, J. A. Scott and N. M. Bedford, *Adv. Mater.*, 2023, **35**, 2305573.
23 L. Lu, C. Wen, H. Wang, Y. Li, J. Wu and C. Wang, *J. Catal.*, 2023, **424**, 1–8.
24 Y. Lu, C.-L. Dong, Y.-C. Huang, Y. Zou, Y. Liu, Y. Li, N. Zhang, W. Chen, L. Zhou, H. Lin and S. Wang, *Sci. China: Chem.*, 2020, **63**, 980–986.
25 Y. Lu, T. Liu, C.-L. Dong, C. Yang, L. Zhou, Y.-C. Huang, Y. Li, B. Zhou, Y. Zou and S. Wang, *Adv. Mater.*, 2022, **34**, 2107185.
26 H. Wang, J. Zhang and S. Tao, *Chem. Eng. J.*, 2022, **444**, 136693.
27 Y.-F. Qi, K.-Y. Wang, Y. Zhou, Y. Sun and C. Wang, *Chem. Eng. J.*, 2023, **477**, 146917.
28 R. Zhong, Q. Wang, L. Du, Y. Pu, S. Ye, M. Gu, Z. Conrad Zhang and L. Huang, *Appl. Surf. Sci.*, 2022, **584**, 152553.
29 R. Zhong, P. Wu, Q. Wang, X. Zhang, L. Du, Y. Liu, H. Yang, M. Gu, Z. C. Zhang, L. Huang and S. Ye, *Green Chem.*, 2023, **25**, 4674–4684.
30 F. Chu, B. Lu, G. Zhao, Z. Zhu, K. Yang, T. Su, Q. Zhang, C. Chen and H. Lü, *ChemSusChem*, 2023, e202301385.
31 Y. Song, K. Ji, H. Duan and M. Shao, *Exploration*, 2021, **1**, 20210050.
32 M. Zhang, Y. Liu, B. Liu, Z. Chen, H. Xu and K. Yan, *ACS Catal.*, 2020, **10**, 5179–5189.
33 W. Song, Y. Xu, X. Xie, C. Li, W. Zhu, Q. Xiang, W. Chen, N. Tang and L. Wang, *ACS Appl. Mater. Interfaces*, 2023, **15**, 27253–27263.
34 G. Liu, T. Nie, Z. Song, X. Sun, T. Shen, S. Bai, L. Zheng and Y.-F. Song, *Angew. Chem., Int. Ed.*, 2023, **62**, e202311696.
35 G. Li, Y. Xu, H. Pan, X. Xie, R. Chen, D. Wu and L. Wang, *J. Mater. Chem. A*, 2022, **10**, 6748–6761.
36 A. C. Bouali, M. Serdechnova, C. Blawert, J. Tedim, M. G. S. Ferreira and M. L. Zheludkevich, *Appl. Mater. Today*, 2020, **21**, 100857.
37 G. E. de O. Blanco, C. W. O. de Souza, M. P. Bernardo, M. Zenke, L. H. C. Mattoso and F. K. V. Moreira, *Mater. Today Commun.*, 2021, **27**, 102169.
38 B. Liu, S. Xu, M. Zhang, X. Li, D. Decarolis, Y. Liu, Y. Wang, E. K. Gibson, C. R. A. Catlow and K. Yan, *Green Chem.*, 2021, **23**, 4034–4043.
39 Y. Song, Z. Li, K. Fan, Z. Ren, W. Xie, Y. Yang, M. Shao and M. Wei, *Appl. Catal., B*, 2021, **299**, 120669.
40 R. Zheng, C. Zhao, J. Xiong, X. Teng, W. Chen, Z. Hu and Z. Chen, *Sustainable Energy Fuels*, 2021, **5**, 4023–4031.
41 Y. Li, Y. Xu, C. Li, W. Zhu, W. Chen, Y. Zhao, R. Liu and L. Wang, *Molecules*, 2023, **28**, 1173.
42 X. Li, Z. Zhang, Q. Xiang, R. Chen, D. Wu, G. Li and L. Wang, *RSC Adv.*, 2021, **11**, 12392–12397.
43 Y. Gan, Z. Li, Y. Ye, X. Dai, F. Nie, X. Yin, Z. Ren, B. Wu, Y. Cao, R. Cai, X. Zhang and W. Song, *ChemSusChem*, 2022, **15**, e202201205.
44 A. Zhang, W. Zheng, Z. Yuan, J. Tian, L. Yue, R. Zheng, D. Wei and J. Liu, *Chem. Eng. J.*, 2020, **380**, 122486.
45 X. Deng, X. Kang, M. Li, K. Xiang, C. Wang, Z. Guo, J. Zhang, X.-Z. Fu and J.-L. Luo, *J. Mater. Chem. A*, 2020, **8**, 1138–1146.
46 S. Guo, M. Ma, R. Ge, H. Algadi and Q. Shao, *Adv. Compos. Mater.*, 2023, **6**, 158.
47 X. Fu, Y. Chen, T. Wang, Z. Li, Y. Lei and S. Kawi, *Int. J. Hydrogen Energy*, 2022, **47**, 27996–28006.
48 S. Zhu, Z. Wang, F. Huang, H. Zhang and S. Li, *J. Mater. Chem. A*, 2017, **5**, 9960–9969.
49 X. Zhang, J. Zhou, W. Dou, J. Wang, X. Mu, Y. Zhang, A. Abas, Q. Su, W. Lan, E. Xie and C. Zhang, *J. Power Sources*, 2018, **383**, 124–132.
50 R. Tong, M. Xu, H. Huang, C. Wu, X. Luo, M. Cao, X. Li, X. Hu, S. Wang and H. Pan, *Int. J. Hydrogen Energy*, 2021, **46**, 39636–39644.
51 Y. Cao, T. Wang, X. Li, L. Zhang, Y. Luo, F. Zhang, A. M. Asiri, J. Hu, Q. Liu and X. Sun, *Inorg. Chem. Front.*, 2021, **8**, 3049–3054.
52 M. T. Bender, Y. C. Lam, S. Hammes-Schiffer and K.-S. Choi, *J. Am. Chem. Soc.*, 2020, **142**, 21538–21547.

53 B. J. Taitt, D.-H. Nam and K.-S. Choi, *ACS Catal.*, 2019, **9**, 660–670.
54 D.-H. Nam, B. J. Taitt and K.-S. Choi, *ACS Catal.*, 2018, **8**, 1197–1206.
55 C. Wang, Q. Zhang, Z. Liu, B. Li, W. Zhao, C. Zhang, S. Jiang, J. Wang, K. Liu and S. He, *ChemSusChem*, 2024, e202301703.
56 T. Guo, K. Xiang, X. Wen, W. Zhou and H. Chen, *Mater. Res. Bull.*, 2024, **170**, 112595.
57 Y. Liu, K. Xiang, W. Zhou, W. Deng, H. Zhu and H. Chen, *Small*, 2023, 2308741.
58 N. Zhang, Y. Zou, L. Tao, W. Chen, L. Zhou, Z. Liu, B. Zhou, G. Huang, H. Lin and S. Wang, *Angew. Chem., Int. Ed.*, 2019, **58**, 15895–15903.
59 H. G. Cha and K.-S. Choi, *Nat. Chem.*, 2015, **7**, 328–333.
60 T. Wang, L. Tao, X. Zhu, C. Chen, W. Chen, S. Du, Y. Zhou, B. Zhou, D. Wang, C. Xie, P. Long, W. Li, Y. Wang, R. Chen, Y. Zou, X.-Z. Fu, Y. Li, X. Duan and S. Wang, *Nat. Catal.*, 2022, **5**, 66–73.
61 R. Peng, Y. Jiang, C.-L. Dong, T. T. Thuy Nga, Y. Lu, S. Li, Y. Fan, C. Xie, S. Wang and Y. Zou, *J. Mater. Chem. A*, 2023, **11**, 15196–15203.